Lithos 376–377 (2020) 105714

Contents lists available at ScienceDirect

Lithos

journal homepage: www.elsevier.com/locate/lithos

Research Article

Generation and exhumation of granitoid intrusions in the Penjween ophiolite complex, NW Zagros of the Kurdistan region of Iraq: Implications for the geodynamic evolution of the Arabian-Eurasian collision zone

Sabah A. Ismail [a,*], Renas I. Koshnaw [b], Douglas E. Barber [c], Heider Al Humadi [d], Daniel F. Stockli [c]

[a] Applied Geology Department, College of Sciences, Kirkuk University, Kirkuk, Iraq
[b] Department of Structural Geology and Geodynamics, Geoscience Center, University of Göttingen, Goldschmidtstraße 3, Göttingen 37077, Germany
[c] Department of Geological Sciences, Jackson School of Geosciences, University of Texas at Austin, Austin 78712, TX, USA
[d] Department of Geography and Geology, University of Turku, 20014, Finland

ARTICLE INFO

Article history:
Received 15 June 2020
Received in revised form 22 July 2020
Accepted 25 July 2020
Available online 31 July 2020

Keywords:
Neotethys
Ophiolite
Geochronology
Thermochronology
Zagros
Iraq

ABSTRACT

The Penjween ophiolite complex represents a remnant of the Neotethys oceanic crust that was preserved in the Zagros Suture Zone of NE Iraq. The complex is composed of dunite, harzburgite, and pyroxenite at the bottom, gabbro in the middle, and diorite at the top. Minor peraluminous granitiod intrusions of different types were identified in the complex. These granitoids are classified into trondhjemite and pegmatitic granite. Zircon grains from these intrusions show different ages and geochemistry, pointing at differences in their genesis and composition of the parent melts. The trondhjemite has an age of ~90 Ma giving the minimum age of the ultramafic section. This indicates that the mafic rocks were underlain by a source capable of yielding silica-saturated sodic granitoids. The pegmatitic granite with high potassium content, has a U—Pb zircon age of ~46 Ma, suggesting derivation from a non-mafic source melt at a younger age. The (U—Th)/(He—Pb) double dating on zircons from the trondhjemite and pegmatitic granite intrusions indicate a comparable exhumation age of ~23 Ma. These results suggest that two episodes of magmatism occurred prior to the final closure of the Neotethys. In the Late Cretaceous event, melting of a mafic source formed trondhjemites, whereas in the middle Eocene event, possibly melting of the associated sedimentary rocks with the downgoing Neothethys oceanic slab formed pegmatitic granite. The similar exhumation time of the two genetically different granitoids suggests that the Penjween ophiolite complex was exhumed by the beginning of Miocene, potentially as a consequence of the Arabian-Eurasian plate collision.

1. Introduction

The Zagros orogenic belt represents the central part of the Alpine-Himalayan orogenic system. It is a ~2000 km long belt that extends from the East Anatolian Fault in southeastern Turkey and continues through northeastern Iraq to the Makran Subduction Zone in southern Iran (Alavi, 1994; Dercourt et al., 1986; Falcon, 1974) (Fig. 1). The Zagros orogenic belt formed by three major tectonic events: Early to Late Cretaceous subduction of the Neotethyan oceanic plate beneath the Eurasian continental plate, emplacement of the Late Cretaceous Neotethyan ophiolites on the Arabian continental passive margin, and the Cenozoic collision of the Arabian and Eurasian continental plates (Alavi, 1994; Agard et al., 2005; Al Humadi et al., 2019; Shafaii Moghadam et al., 2019; Mohajjel and Ferguson, 2014; Shafaii Moghadam and Stern, 2015). As a young continental convergence zone, the Zagros orogenic belt provides an opportunity to assess the tectonic cycle processes of subduction, obduction, and continental collision. The Zagros orogenic belt in the study area illustrates an intermediate phase between the preliminary obduction stages that is preserved along the Makran–Oman transect and the late stage collision that observed in southeastern Turkey (Agard et al., 2005; Shafaii Moghadam et al., 2014; Fergusson et al., 2016). The rock record in the Iraqi Zagros segment preserves phases of subduction and collision in association with the extensive Cenozoic magmatism in the Zagros Suture Zone (ZSZ; Jassim and Goff, 2006). The Iraqi ophiolite complexes along the ZSZ are distributed discontinuously, marking the boundary between the Arabian and the Eurasian continental plates. These ophiolite complexes represent remnants of the southern Neotethyan oceanic crust that was obducted in two major tectonic events during the Late Cretaceous and the Paleogene, by a series of collisions of intra-oceanic arc-trench systems with the Arabian continental margin (Ismail et al.,

* Corresponding author.
E-mail address: sabah@uow.edu.au (S.A. Ismail).

https://doi.org/10.1016/j.lithos.2020.105714
0024-4937/

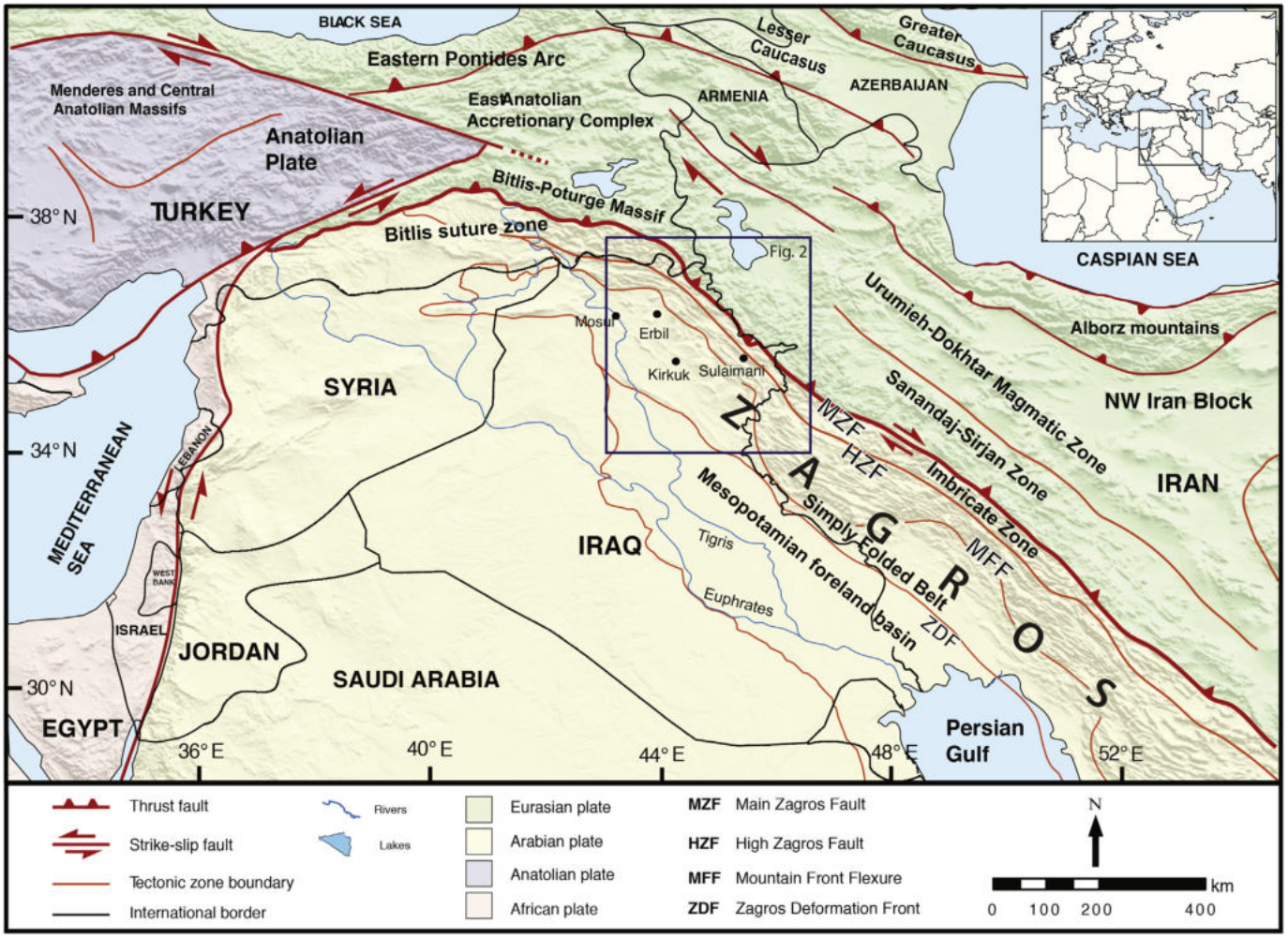

Fig. 1. Regional tectonic map of the Middle East, including the NW Zagros belt in the Kurdistan region of Iraq (modified from Koshnaw et al., 2017).

2014; Ali et al., 2016, 2019). The Mawat, Penjween, Pushtashan, Hasanbag, and Kata-Rash complexes (Fig. 2) have been identified as Mesozoic ophiolites (Ali et al., 2012, 2016, 2019; Abdulla, 2015; Al Humadi et al., 2019). Mélange-like assemblages such as the Rayat, Qalander, and Bulfat complexes have been identified as Cenozoic ophiolites and were preserved as incomplete fragments in association with the Paleogene Walash-Naopurdan groups (Arai et al., 2006; Ismail et al., 2009, 2010, 2014; Ali et al., 2019).

The objective of this study is to determine the geochemical and petrological characteristics as well as, the timing of generation and exhumation of the Penjween ophiolite complex to unravel the subduction and subsequent collision history of the ZSZ in Iraq. In addition to the whole-rock geochemistry of the granitoid intrusions in the Penjween ophiolite complex, the (U—Th)/(He—Pb) age and trace elements content of their zircons will also be presented.

2. Geologic background

Many researchers have studied the tectonic history of the Zagros orogenic belt in Iraq, including the ZSZ, fold-thrust belt, and foreland basin (Buday and Jassim, 1987; Al-Kadhimi et al., 1996; Numan, 1997; Jassim and Goff, 2006; Al-Qayim et al., 2012; Lawa et al., 2013; Ali et al., 2014, 2019; Koshnaw et al., 2017, 2018, 2019). The geology and tectonics of Iraq is subdivided into three major zones: (1) the Zagros Suture Zone in the northeastern extremity of Iraq, (2) the Unstable Shelf, encompassing the northern and east-central part of Iraq, and (3) the Stable Shelf that includes the central and western parts of Iraq (Buday and Jassim, 1987). The principal tectonic units in Iraq generally trend NW-SE, parallel to the Zagros structures of Iraq and Iran and E-W, parallel the Tauride structures of SE Turkey. Development of the Zagros Suture and Unstable Shelf zones was affected by the Cenozoic collision, whereas the Stable Shelf was influenced by the tectonic history of the Arabian craton. The ZSZ was subdivided by Jassim and Goff (2006) into three zones: the Qulqula-Khwakurk Zone, the Penjween-Walash Zone, and the Shalair Zone (Fig. 2).

The Qulqula-Khwakurk Zone comprises mostly the sedimentary units of southern Neotethys that were folded and sutured to the Arabian plate during the Late Cretaceous (Jassim and Goff, 2006). The sedimentary units from this zone mainly consist of the Triassic Avroman limestone, the Triassic–Cretaceous Qulqula deep marine radiolarian chert, mudstone, and limestone that are succeeded by the Albian-Cenomanian conglomerate. Basaltic flows and dykes occur in these sequences, yet no absolute ages and geologic descriptions are available on them. The Penjween-Walash Zone extends along the Iraq-Iran border and includes the main Neotethys ophiolites (Fig. 2). This zone contains three allochthonous thrust sheets: Naopurdan at the bottom, Walash in the middle, and Gimo-Qandil at the top. Both the Walash and the Naopurdan thrust sheets contain Paleogene ophiolite rocks (Ismail et al., 2014). The Walash and Naopurdan sheets are structurally overlain by the Cretaceous Gimo-Qandil sheet. The Gimo-Qandil sheet contains mafic and ultramafic massifs, representing dismembered Late Cretaceous ophiolites of the Penjween, Mawat, and Pushtashan complexes (Fig. 2).

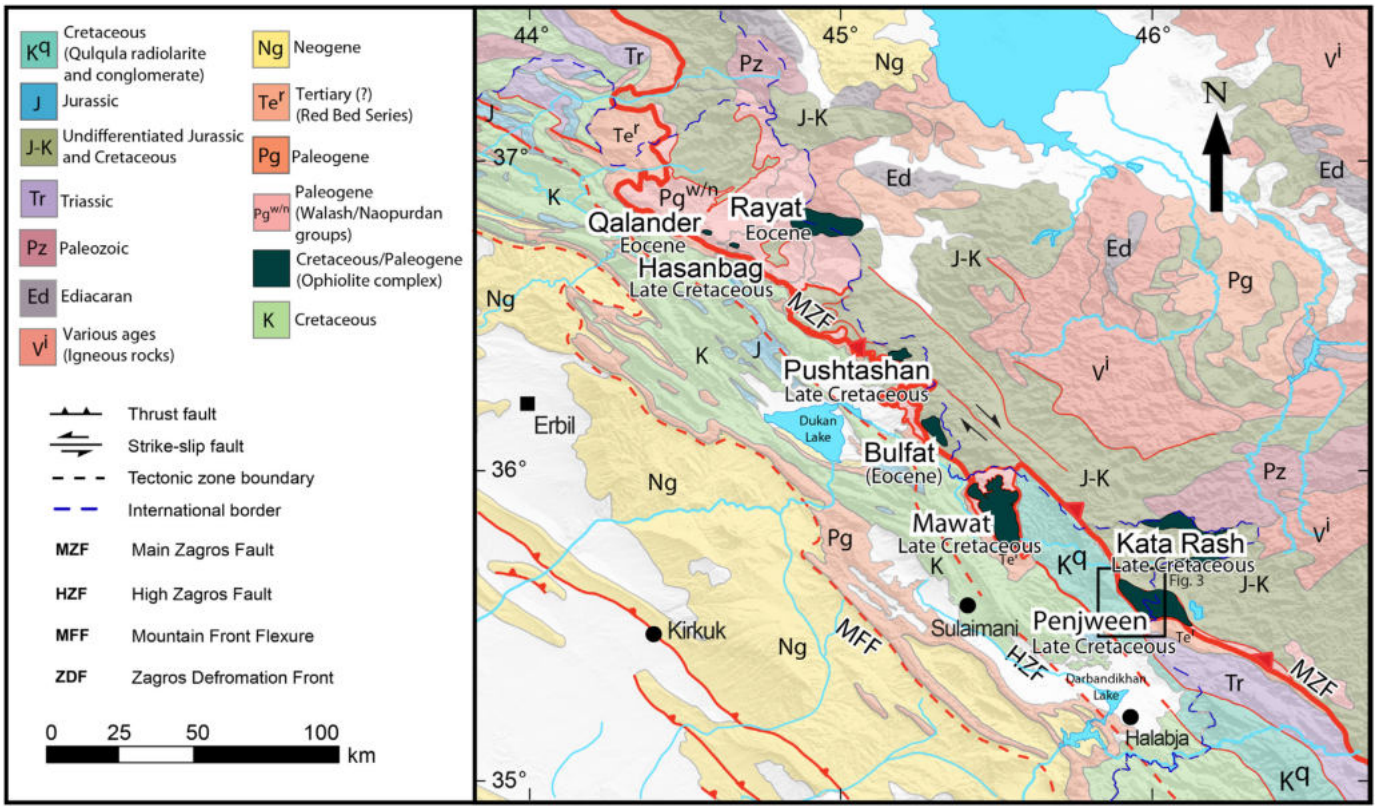

Fig. 2. Regional geologic map of the northeastern Iraq and northwestern Iran showing the major tectonic subdivisions, major rocks units, and locations of the Zagros ophiolitic terranes (Al-Kadhimi et al., 1996; Koshnaw et al., 2017; Ali et al., 2019).

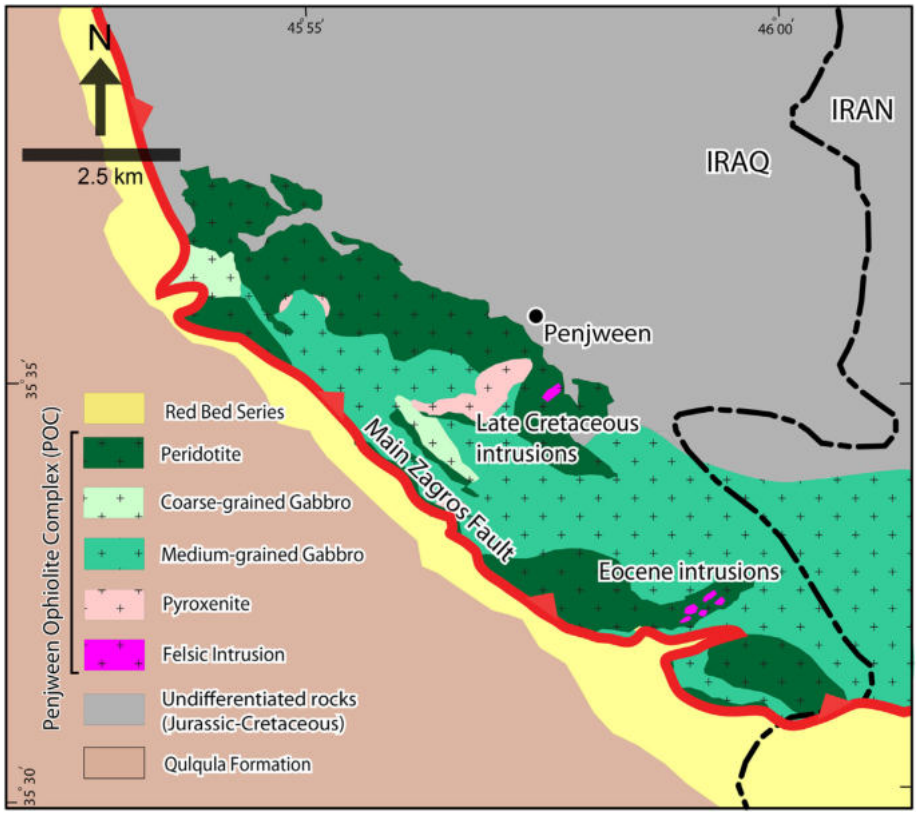

Fig. 3. Simplified geologic map of the Penjween ophiolite complex and the surrounding areas showing the pegmatitic granite and trondhjemite intrusions (modified from Jassim and Goff, 2006).

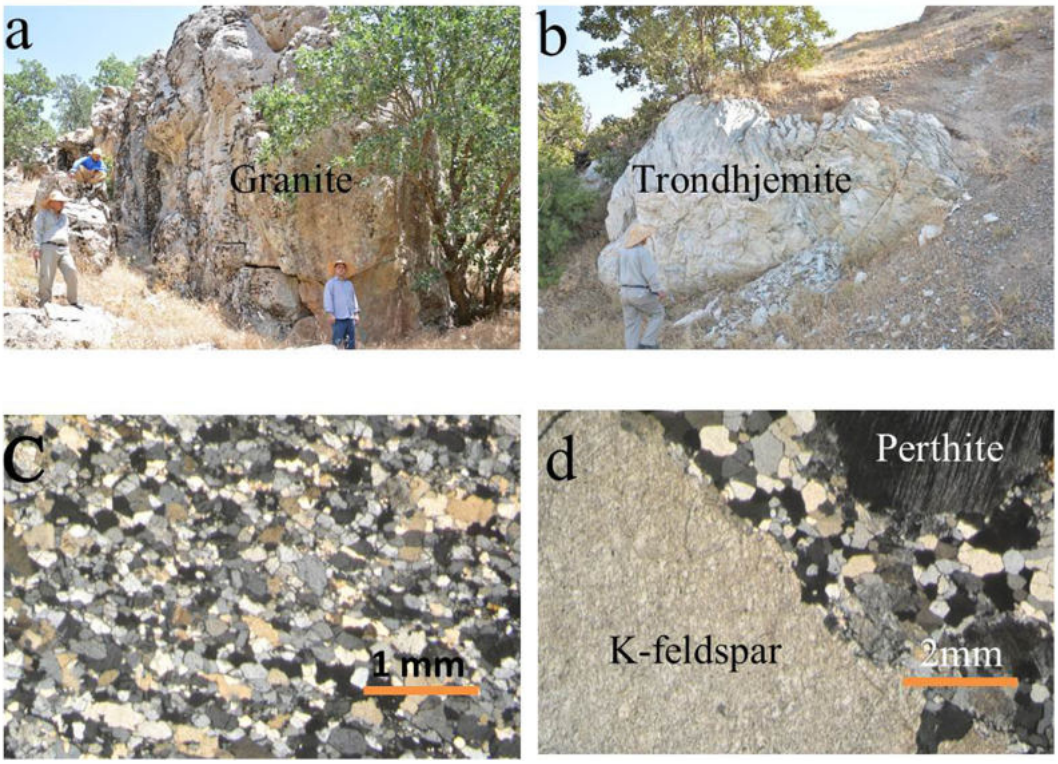

Fig. 4. Field views of the studied granitoid bodies that intruded into the mantle peridotites of the Penjween ophiolite complex. (a) Pegmatitic granite intrusion. (b) Trondhjemite intrusion. (c) Photomicrograph showing hypidiomorphic granular texture with medium-grained quartz and plagioclase minerals (0.3–1 mm). (d) Photomicrograph showing porphyritic texture between K-feldspars, quartz and rare plagioclase in the pegmatitic granite intrusions.

Structurally, the Shalair Zone is the highest thrust sheet within the Iraqi segment of the Zagros orogenic belt (Fig. 2). The Shalair Zone is considered as a part of the Sanandaj-Sirjan Zone (Jassim and Goff, 2006). The rocks of this zone are mainly metamorphosed Upper Permian rocks that are overlain by the Jurassic and Lower Cretaceous fore-arc metasediments and the Upper Cretaceous calc- alkaline andesitic rocks (Kata Rash unit) with imbricated slices of the Upper Triassic deep water carbonate rocks (Jassim and Goff, 2006).

The Penjween ophiolite complex (POC), within the Penjween-Walash Zone, is ~16 km long and ~5 km wide that trends NW-SE parallel to the regional structures and continues into the Iranian Zagros segment (Fig. 3). The POC is bounded by phyllite and calc-schist of the Cretaceous metamorphosed Gimo group to the east and by the Cenozoic clastic Red Bed Series to the west (Fig. 3; Jassim and Goff, 2006). The POC was thrusted onto the Red Bed Series deposits during the Miocene-Pliocene (Al Hassan and Hubbard, 1985; Buday and Jassim, 1987; Jassim and Goff, 2006). The POC is thrusted over by the metamorphosed Late Cretaceous volcano-sedimentary units of the Penjween group. The POC is composed of dunite, harzburgite and pyroxenite at the bottom, to gabbro and diorite at the top. These three rock units are separated by thrusts (Jassim and Goff, 2006; Al-Qayim et al., 2012; Ali et al., 2019). Dunite rocks occur either as small massive lenses or as envelopes surrounding chromitite ore bodies. The contact between the dunite lenses and their host peridotite is sharp, whereas the dunite envelopes around the chromitites grade outward into harzburgite. Harzburgite is the most abundant rock in the Penjween ultramafic body which consists of forsteritic olivine and Mg-rich orthopyroxene and minor chromite; these minerals underwent different degrees of alteration. Pyroxenite occurs as two types: (1) as small bodies, usually near the contact of peridotite and gabbro, and (2) as dykes cutting mafic and ultramafic rocks. Volcanic rocks of this complex are exposed over a width of ~20 km, oriented northwest-southeast (Buday and Jassim, 1987). They consist of basalts, basaltic tuffs and andesite. Minor felsic intrusions comprise <0.5% of the Penjween ophiolite sequence. These were intruded into the mantle rocks in several locations.

3. Petrography of the Penjweeen granitoid intrusions

White-colored trondhjemite and pegmatitic granite were found at eleven localities in the upper part of the mantle section of the POC. The thickness of the trondhjemite bodies ranges between 1 and 3 m. The pegmatitic granite bodies are larger, and extend up to 50 m across (Fig. 4A and B). Sharp contacts were observed between the trondhjemite and the host peridotites, whereas an amphibolite body separates the pegmatitic granite from its host peridotite rocks. Petrographic studies were conducted on 22 thin sections from these granitoid intrusions (trondhjemite and pegmatitic granite). The trondhjemite is a leucocratic rock that consists predominantly of quartz, plagioclase and lesser orthoclase (Fig. 4C); they have hypidiomorphic granular texture with a medium grain size (0.3–1 mm) and are classified as tonalite-trondhjemite. They also show a schistosic texture as alternation of fine-grained and medium-grained aggregates. Apatite, rutile, monazite and zircon grains form tiny accessory minerals. Plagioclases are subhedral with a medium-grain size of (0.5–1 mm) and are partly transformed to epidote. Quartz is generally anhedral and rarely displays recrystallization textures. The rocks are variably altered, containing different secondary minerals such as epidote and chlorite. Primary biotite is commonly replaced by chlorite. Most of the original pyroxene is replaced by amphibole. These modifications suggest that the trondhjemite rocks were either affected by hydrothermal alteration (Spooner and Fyfe, 1973; Lecuyer et al., 1990) or experienced weak greenschist facies metamorphism (Coleman and Donato, 1979).

The pegmatitic granite intrusions consist mainly of K-feldspars, quartz and rare plagioclase. The feldspars are mostly orthoclase, forming very large crystals and occasionally showing perthite twins. Additionally, these feldspars are characterized by a porphyritic texture with euhedral to subhedral orthoclase phenocrysts surrounded by groundmass of fine-grained plagioclase, quartz, and biotite. Features such as bending of orthoclase cleavage and twin planes, and undulose extinction indicate mild deformation after crystallization. The feldspars are slightly kaolinized. The quartz grains are well-developed crystal with wavy extinction, but smaller in size relative to the feldspars. Aggregates of fine-grained feldspar that are mixed with less quartz were likely produced as a result of stress effect, causing cataclastic deformation. Quartz veinlets within the cleavage planes of the deformed feldspars were likely produced by shearing. The shearing is also observed by the presence of oriented thin streaks of muscovite bundles that traverses the rock. Tourmaline, zircon, monazite and ilmenite occur as accessory minerals.

Table 1
Major, trace and rare earth elements concentrations of the Penjween granitoid intrusions.

Rock type	Trondhjemite				Pegmatitic granite		
Sample no.	Pnj3	Pnj9	Pnj10	Pnj11	AA2	pnj6	PnjBB2
Major oxide (wt%)							
SiO_2	68.81	68.84	71.01	66.05	75.02	74.7	73.5
TiO_2	0.16	0.14	0.09	0.14	0.06	0.04	0.05
Al_2O_3	18.44	17.99	18.4	19.69	13.47	14.2	13.72
FeO_{tot}	0.5	0.98	0.45	1.56	1.55	1.12	1.42
MnO	0.01	0.02	0.01	0.02	0.01	0.01	0.01
MgO	0.23	1.03	0.21	1.01	0.15	0.14	0.12
CaO	1.71	2.44	1.33	2.87	0.18	0.42	0.22
Na_2O	8.98	7.88	8.03	8.17	3.01	3.73	4.31
K_2O	0.02	0.13	0.12	0.14	6.39	4.87	5.94
P_2O_5	0.02	0.03	0.02	0.08	0.05	0.05	0.05
LOI	0.35	0.2	0.19	0.58	0.48	0.75	0.65
Total	99.23	99.68	99.86	100.31	100.37	100.03	99.99
Trace elements (ppm)							
Ba	28.5	46.8	68.8	249	102	184	137
Co	2	2	1	5	0.8	1	1
Cr	12	10	11	10	10	10	10
Cs	0.07	0.02	0.03	0.05	2.1	3.2	1.9
Cu	5	18	6	32	5.8	7.3	6.8
Ga	16.6	13.8	17.8	15.7	20.1	18.5	23.5
Hf	1.9	1.1	1.2	1.6	0.3	0.6	0.4
Mo	1	1	1	1	1.5	1	1
Nb	11.89	13.6	3.8	7.8	16.8	27.2	19.7
Ni	2	3	2	4	2.4	2	2
Pb	2	2	2	2	9.7	6.4	7.5
Rb	1.1	1.8	1.6	1.1	123	110	137
Sr	121.4	144	116	312	28	65	58
Sn	1	5	1	1	5	1	1
Ta	1.6	2.2	1	1.3	1.3	1.5	1.1
Th	4.22	3.4	3.84	6.7	0.8	2.4	1.4
U	1.15	0.21	0.55	0.45	0.8	1.02	0.9
V	6	5	5	11	5	5	5
W	1	3	1	6	1	1	1
Y	11.6	4.7	3.3	8.5	5.7	14	9.4
Zn	2	3	2	5	3	2	2
Zr	68	53	49	66	33	41	38
Rare earth elements (ppm)							
La	21.4	25.4	30.1	43.2	2.3	6.5	4.6
Ce	35.7	41.1	37.7	56.7	3.4	13	9.8
Pr	3.2	3.99	3.05	6.3	0.33	1.44	0.86
Nd	11	13.1	10.7	22.6	1.4	4.2	2.2
Sm	1.95	2.02	1.37	2.9	0.29	0.67	0.58
Eu	0.21	0.32	0.15	0.39	0.13	0.23	0.19
Gd	1.28	1.2	0.77	1.37	0.47	0.86	0.75
Tb	0.22	0.13	0.11	0.19	0.11	0.23	0.18
Dy	1.43	0.63	0.66	1.33	0.73	1.9	1.57
Ho	0.29	0.14	0.15	0.25	0.19	0.42	0.35
Er	0.89	0.38	0.52	0.9	0.54	1.3	1.2
Tm	0.12	0.06	0.08	0.13	0.08	0.18	0.17
Yb	0.94	0.41	0.53	0.98	0.68	1.22	1.12
Lu	0.16	0.08	0.09	0.15	0.08	0.19	0.17

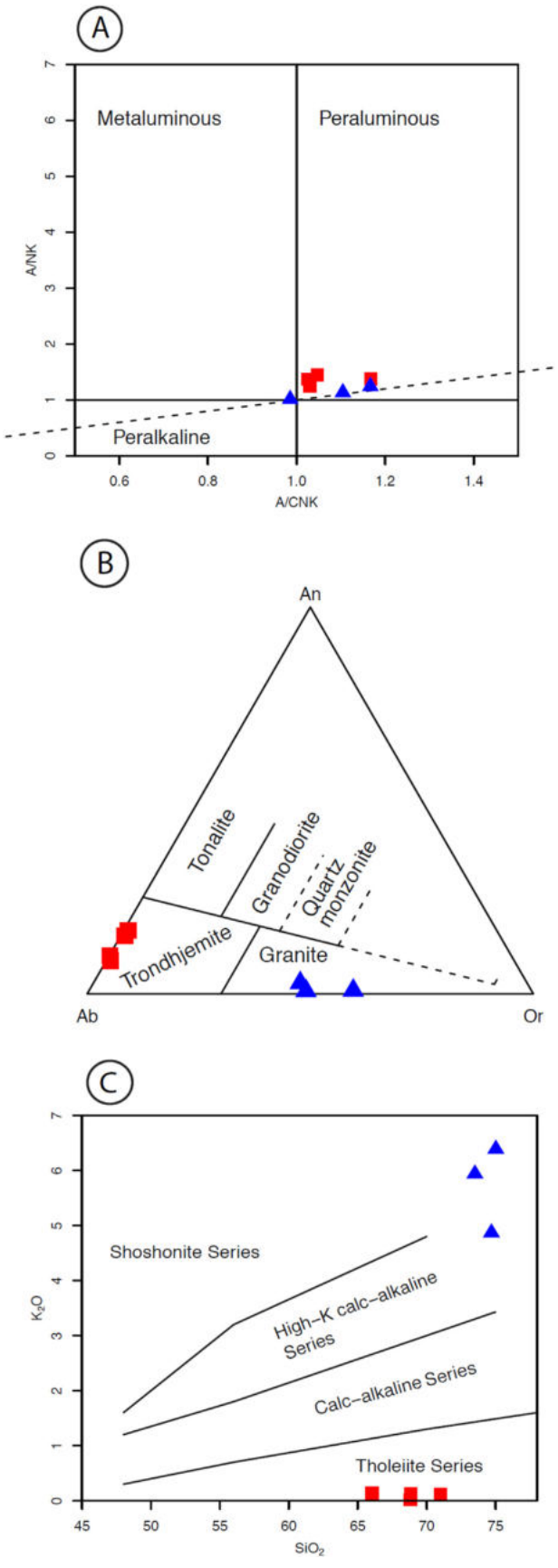

Fig. 5. (A) A/CNK- A/NK plot (Shand, 1943) showing peraluminous composition for the Penjween granitoids (red rectangular for trondhjemite and blue triangle for pegmatite granite). (B) Triplot classification diagram of feldapars (O'Connor, 1965) for the Penjween granitoid intrusions: Group-I, trondhjemite as red rectangular, and Group-II (granite) as blue triangle. (C) K_2O versus SiO_2 plot (after Peccerillo and Taylor, 1976) for the Penjween granitoids; red rectangles for trondhjemite and blue triangles for pegmatitic granite. (For interpretation of the references to colour in this figure legend, the reader is referred to the web version of this article.)

4. Methods

4.1. Whole-rock analysis

The bulk rock major oxides, trace and rare earth elements analysis for 7 samples of the felsic dykes were conducted at Acme Analytical Laboratories Ltd. (Acme) in Vancouver, Canada. The samples were pulverised in a mild steel swing mill and after the $LiBO_2$ fusion and HNO_3 dilution, the major elements, Cr, and Sc were analyzed by inductively coupled plasma-emission spectrometry (ICP-OES). The other trace and rare earth elements were analyzed by inductively coupled plasma-mass spectrometry (ICP-MS). The analytical accuracy and precision were monitored by analyzing the rock reference materials SO-18, SO-19, DS-10, and OREAS45EA. Analytical accuracy has indicated by the relative difference between measured and recommended values, which was better by 2% for the major oxide and 10% for all the other elements (Supplementary Table 1).

4.2. U—Pb, (U—Th)/He age and trace element analyses for zircon

For zircon U—Pb analysis, the separated zircon grains from granitoid samples were put on a double-sided tape mount in order to preserve the grains for later analyses. The grains were unpolished to allow depth profiling and recognition of core versus rim growth (Marsh and Stockli, 2015; Soto-Kerans et al., 2020). The analyses on the zircon grains were conducted at the University of Texas geo- and thermo-chronometry laboratory. The zircon grains were analyzed by the laser ablation inductively coupled plasma mass spectrometry (LA-ICP-MS) using Photon

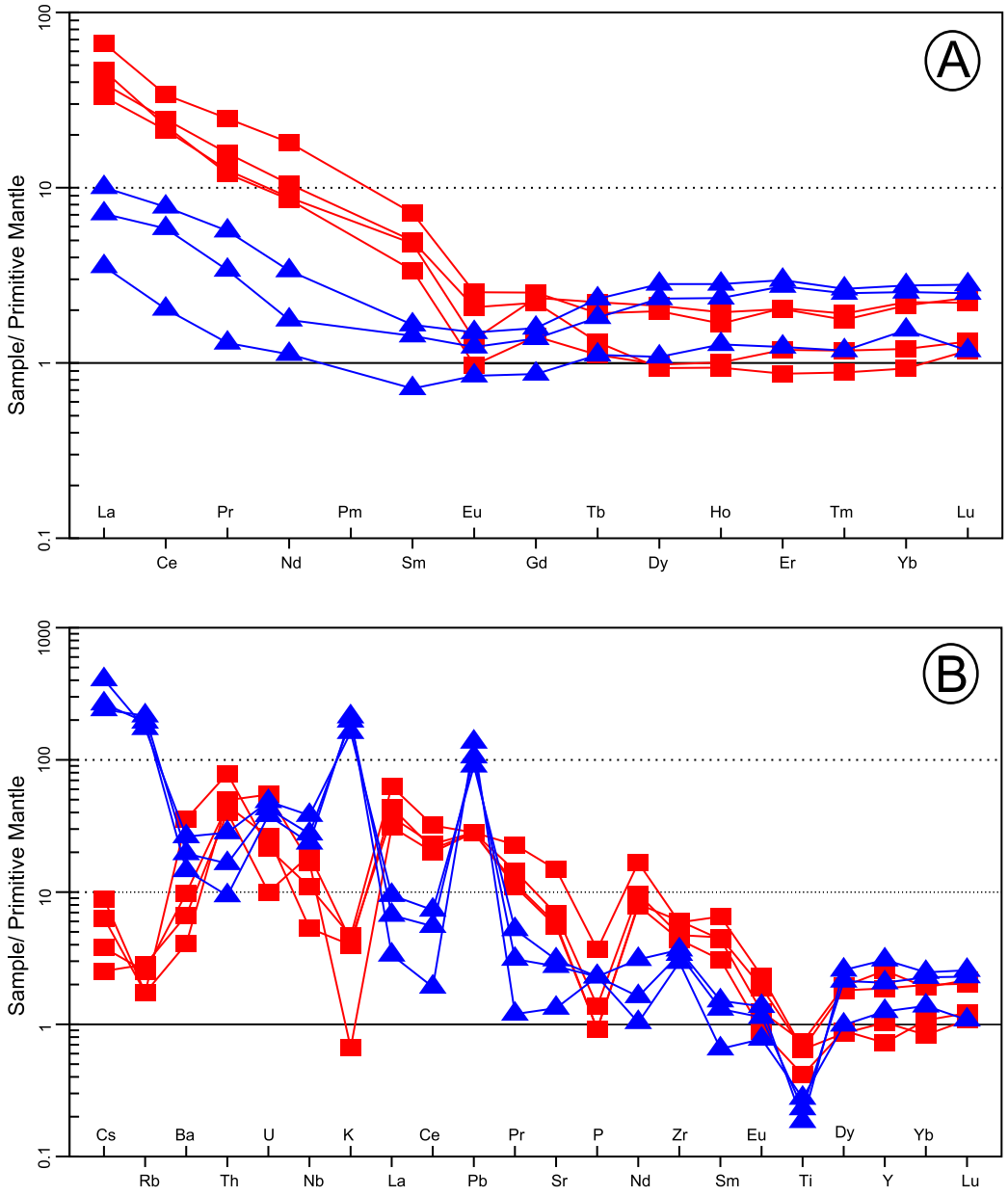

Fig. 6. (A) Primitive mantle-normalized rare earth elements distribution of the Penjween pegmatitic granite (blue triangle) and trondhjemite intrusions (red rectangular); normalization data from McDonough and Sun (1995); (B) N-MORB normalized trace elements distribution of the Penjween pegmatitic granite (blue triangles) and trondhjemite intrusion (red rectangles); normalization data from Sun and McDonough (1989). (For interpretation of the references to colour in this figure legend, the reader is referred to the web version of this article.)

Table 2
Trace elements concentration of zircon grains in the trondhjemite and pegmatittic granite intrusions from the Penjween ophiolite complex.

Sample ID	Ti	Hf	Th	U	Tb	Ta	Y	Nb	Th/U	Eu/Eu*	Yb/Gd	U/Yb
Trace elements in zircons from pegmatitic granite (ppm)												
AA2-1	2.38	13560	113	1150	3.15	0.22	769	1.02	0.098	0.542	69.692	2.538
AA2-2	1.94	13390	111	1030	2.45	0.3	567	1.39	0.107	0.475	65.235	3.228
AA2-3	1.3	14040	126	1220	3.13	0.19	860	0.95	0.103	0.932	82.193	2.359
AA2-6	5	12540	1470	7010	12.48	3.73	2570	11.26	0.209	0.598	39.409	6.176
AA2-8	0.7	10970	65.7	699	1.45	0.44	383	0.98	0.093	0.821	71.028	3.065
AA2-9	2.1	13730	329	1600	2.63	0.85	576	2.58	0.205	0.629	41.093	6.083
AA2-10	2.8	13420	610	4400	9.3	1.75	2100	3.6	0.138	0.499	44.559	5.116
AA2-11	3.1	12970	267	1690	4.15	0.55	920	1.33	0.158	0.491	52.289	3.894
AA2-12	0.6	11590	104	750	2.61	0.335	625	0.97	0.138	0.254	66.274	2.218
PNJ6-1	0.93	11760	1010	6110	13.04	1.69	2940	4.6	0.165	0.788	37.551	5.534
PNJ6-3	0.6	15010	359	3840	7.05	1.15	1704	3.09	0.093	0.56	51.18	5.21
Trace elements in zircons from trondhjemite (ppm)												
PNJ10-2	6.3	11330	305	778	22	6.98	3750	18.7	0.392	0.417	19.512	0.648
PNJ10-3	0.9	13720	187	1500	15.9	5.67	3820	16.1	0.124	0.265	53.869	0.828
PNJ10-4	4	12540	60	1020	14	3.32	3400	10.4	0.058	0.217	59.169	0.596
PNJ10-5	4.6	7300	70	178	5.89	1	1260	4.96	0.393	0.36	46.204	0.281
PNJ10-6	3.5	12660	97	527	10.2	2.29	2170	7.02	0.184	0.054	51.628	0.474
PNJ11-1	2.95	6910	128.5	397	13.06	1.83	2195	5.9	0.323	0.435	23.414	0.459

Machine Analyte G.2 with a Helex sample cell and Thermo Element2 ICP-MS. The reference standard GJ1 (Jackson et al., 2004) was used to constrain the fractionation correction of the unknown grains. The reported core ages represent $^{206}Pb/^{238}U$ for zircon ages younger than 850 Ma with a discordance of <10%, determined by $^{206}Pb/^{238}U$ versus $^{207}Pb/^{235}U$ ages, and $^{207}Pb/^{206}U$ ages for zircon ages older than 850 Ma with a discordance of <30%, determined by $^{206}Pb/^{238}U$ versus $^{207}Pb/^{206}U$ (Gehrels et al., 2008; Gehrels, 2011). All ages involve 2σ analytical uncertainty. The raw data were reduced by using Iolite™ plug-in on the Wavemetrics Igor Pro™ platform and VizualAge™ data reduction scheme (Paton et al., 2011; Petrus and Kamber, 2012).

Following the U—Pb analysis, a second spot of 20 μm diameter was chosen on the zircon grains for trace-element geochemical analysis by LA-ICP-MS. Masses analyzed include Si^{29}, Ti^{49}, Y^{89}, Ba^{137}, La^{139}, Ce^{140}, Pr^{141}, Nd^{145}, Sm^{147}, Eu^{153}, Gd^{157}, Tb^{159}, Dy^{163}, Ho^{165}, Er^{166}, Tm^{169}, Yb^{172}, Lu^{175}, Hf^{178}, Ta^{181}, Th^{232}, and U^{238}. Glass NIST612 was used as a primary reference material and Si^{29} as internal standard.

For the purpose of zircon (U—Th)/(He—Pb) double dating, after completion of the U—Pb and trace-elemental analyses, the zircon grains were manually picked from the tape mount and packed in a platinum (Pt) pocket for thermochronometric analysis, following procedures outlined by Wolfe and Stockli (2010). The packed zircon grains were laser heated for 10 min at ~1300 °C to degas them. The released gas impaled with ^{3}He tracer and measured by quadrupole noble gas mass spectrometer. Later the zircon grains unwrapped from the Pt pocket, spiked with ^{230}Th, ^{235}U, ^{149}Sm and REE tracer and put in pressurized digestion vessels with HF-HNO3 mixture and 6 N HCL, each at different stage. Then, the spiked solution was run through Thermo Element2 ICP-MS to measure the concentration of the parent nuclides and contrasted against a gravimetric 1 ppb U–Th–Sm–REE normal solution (Wolfe and Stockli, 2010). The presented zircon helium ages in this study are alpha ejection corrected (Farley et al., 1996) with standard procedure uncertainty of ~8% and 2σ, depending on the used Fish Canyon Tuff standard (Reiners et al., 2002). More details on these methods of zircon U—Pb, (U—Th)/He, and trace element analysis are described in Barber et al. (2019).

5. Results

5.1. Geochemistry of the Penjween granitoid intrusions

Seven granitoid samples from the Penjween ophiolite complex were analyzed (Table 1). All samples are peraluminous with A/CNK ratio of 1.31–1.91 (Fig. 5A) and variably high in Al_2O_3 (13. 47–19.69 wt%) and

Table 3
Rare earth elements concentration for zircon grains from the trondhjemite and pegmatitic granite intrusions of the Penjween ophiolite complex.

Sample ID	La	Ce	Pr	Nd	Sm	Eu	Gd	Dy	Ho	Er	Tm	Yb	Lu
Rare earth elements in zircons from pegmatite granite (ppm)													
AA2-1	0.0015	1.92	0.0099	0.063	0.47	0.31	6.5	55.9	25.1	141	40.7	453	92.2
AA2-2	0.046	1.87	0.0221	0.21	0.55	0.255	4.89	43.4	18.9	99	28.8	319	61.8
AA2-3	0.002	1.78	0.0111	0.124	0.48	0.53	6.29	60.4	27.2	155	44.9	517	106
AA2-6	0.071	12.93	0.116	1.08	2.62	1.7	28.8	201	83.9	434	111.6	1135	200
AA2-8	0.0054	1.53	0.0069	0.128	0.19	0.21	3.21	26.9	12.09	68.4	20.1	228	41.5
AA2-9	0.015	2.8	0.02	0.38	0.62	0.41	6.4	45.4	18.4	99	26	263	50.7
AA2-10	0.048	5	0.062	0.49	1.68	0.93	19.3	157	66	361	90	860	172
AA2-11	0.0034	2.57	0.0115	0.081	0.9	0.44	8.3	72	29.4	163	42.8	434	89
AA2-12	0.004	1.91	0.0024	0.155	0.41	0.12	5.1	43.2	19.7	110	30.1	338	69
PNJ6-1	0.57	19.6	0.45	1.83	3.04	2.44	29.4	210	90.4	465	113.8	1104	221
PNJ6-3	0.002	4.16	0.0105	0.36	1.1	0.73	14.4	121.8	53	284	73.9	737	151
Rare earth elements in zircons from trondhjemite (ppm)													
PNJ10-2	0.134	26.3	0.199	3.52	8.5	3.12	61.5	317	124.5	578	132.4	1200	245
PNJ10-3	0.022	5.36	0.046	0.6	2.59	0.81	33.6	270	120.3	689	175	1810	376
PNJ10-4	12	8	0.5	2.3	3.08	0.67	28.9	238	109	624	162	1710	354
PNJ10-5	0.064	4.49	0.05	0.58	1.59	0.55	13.7	94	41.8	234	59.6	633	140
PNJ10-6	0.125	2.77	0.075	0.81	2.9	0.14	21.5	168	72	414	106	1110	232
PNJ11-1	0.011	10.17	0.183	3.26	5.94	2.11	36.9	165.6	67.2	342	85.9	864	171.2

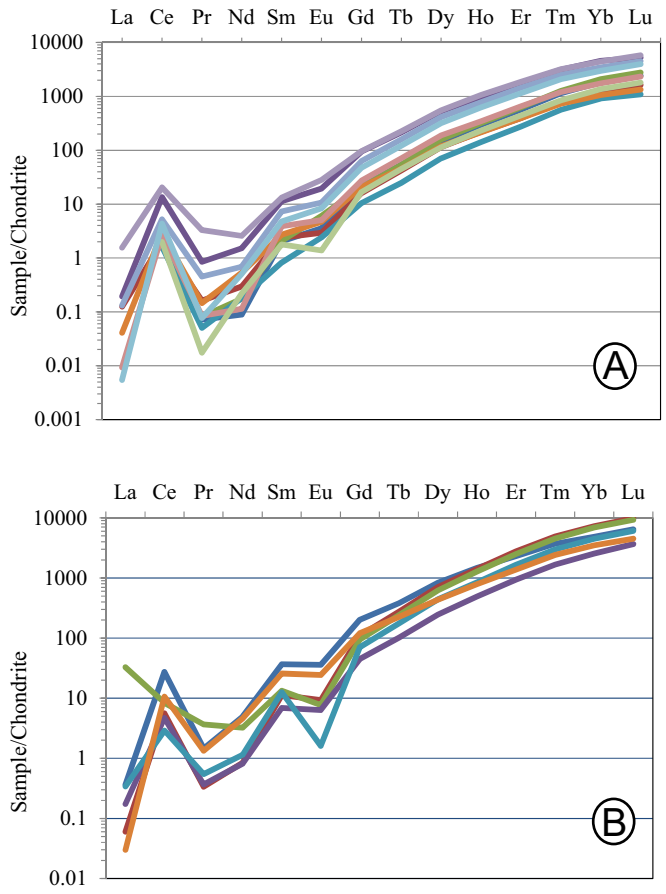

Fig. 7. Chondrite-normalized REE patterns for pegmatitic granite (A) and trondhjemite (B).

Na_2O (3.01–8.98 wt%) contents. The majority of samples ≤ 0.75 wt% LOI, indicating low degree of alteration. Based on the geochemical characteristics, the granitoids can be subdivided into two groups. Samples from group I have low SiO_2 contents of 66–71 wt%, whereas those from group II have high SiO_2 contents of 73.5–75 wt%. According to the triplot classification diagrams of feldspars (O'Connor, 1965), group I classifies as trondhjemite and group II as granite (Fig. 5B). The group-I trondhjemites have high Sr (116–312 ppm) and low Y (3.3–11.6 ppm) contents, with a high Sr/Y ratio of 10.46–36.7. Additionally, the primitive mantle-normalized group-I trondhjemites display fractionated REE patterns showing a negative slope for the LREE (La to Gd) and a flat trend for the HREE (Tb to Lu) (Fig. 6A) with negative Eu anomalies ($Eu/Eu^* = 0.38–0.52$). The group-II granites contain low Sr (28–65 ppm) and Y (5.7–14 ppm) and have less fractionated REE patterns showing a negative slope for LREE and a flat trend for HREE with low LREE values and no clear Eu anomalies. Group-I trondhjemites are richer in LREE ($La_N/Yb_N = 15.38–41.94$ and $La_N/Sm_N = 6.9–13.82$) than the group-II granites ($La_N/Yb_N = 2.28–3.59$ and $La_N/Sm_N = 4.99–6.1$). The primitive mantle-normalized spider diagrams for trace elements, group-I trondhjemites have distinct humps for Th, La, and Nd and troughs for Rb, K, P and Ti (Fig. 6B). In contrast, group-II granites show a general negative pattern with distinct humps for Cs, K and Pb and troughs for Th, Ce and Ti.

5.2. Trace elements in zircon

The behavior and distribution of trace elements in the zircon grains are of great importance in identification of their genetic origin (Hoskin and Schaltegger, 2003; Whitehouse and Platt, 2003). The integration of trace elements into the magmatic zircon grains is controlled by pressure, temperature, and composition of the parent melts as well as the diffusivity of the trace elements in the crystal and melts (Reiners et al., 2005; Rubatto and Hermann, 2007). The trace elements content in zircon from the granitoid of the POC provide the absolute level of each element and their variation between the group-I trondhjemites and group-II pegmatitic granite (Table 2). Zircon grains from the granitoid intrusions have high Th/U ratios of 0.1–0.4, indicating a magmatic origin for both types of zircons (Hoskin and Schaltegger, 2003). The highest combined content of U and Th occurs in the zircon grains from the pegmatitic granite (8480 ppm), whereas the lowest content of 248 ppm is in the trondhjemite. The highest Hf value of 1.5 wt% is found in the zircon grains of the pegmatitic granite; whereas the lowest value of 0.69 wt% is in the zircon grains of the trondhjemite. The lowest average concentrations of Y value of 1247 ppm was found in the zircon grains of the pegmatitic granite, whereas the highest average value of 2766 ppm was in the zircon grains of the trondhjemites. The Hf/Y ratio in the zircon grains from the trondhjemites and pegmatitic granite is ≤4 and >10, respectively. The Ti content of 3.7 ppm in the zircon grains which is highly sensitive to the formation temperature (Fu et al., 2008), ranges between <1 and 9.8 ppm. The average Ti content of 3.7 ppm is high in the zircon grains of trondhjemite. The Sr content in zircon grains is ~11 ppm. Zircon grains from the pegmatitic granite and trondhjemite samples exhibit limited variation in the concentrations of Nb and Ta. The Nb/Ta ratio of zircon grains varies from 2.22 to 5 with an average of 3.2. These elements generally behave incompatibly in the granitic melts and become concentrated in the residual liquid (Linnen et al., 2014).

5.3. REEs in Zircon

The rare earth element (REE) content in the analyzed zircon grains show significant differences between the two studied groups (group-I trondhjemites and group-II pegmatitic granite) (Table 3). The total concentrations of REEs in the zircon grains from the trondhjemite samples (1223–3483 ppm) are significantly higher than those from the pegmatitic granite samples (513–2261 ppm). The chondrite-normalized REE patterns of zircon grains from the pegmatitic granite and trondhjemite samples show similar positive slope with distinct positive Ce anomalies and slight negative Eu anomalies (Fig. 7A, B); the negative Eu anomaly is more distinct in in the zircon grains from trondhjemites (Fig. 7B). The positive Ce-anomaly of zircon grains is interpreted as a magmatic signature that resulted from the preferential incorporation of Ce^{4+} into the structure of zircon crystals (e.g. Hanchar and Westrenen, 2007), implying oxidizing conditions during zircon crystallization (Hinton and Upton, 1991). In spite of the variation in the REE contents in the zircon grains, the chondrite-normalized REE patterns (Sun and McDonough, 1989), from both trondhjemite and pegmatitic granite are similar with approximately parallel trends (Fig. 7).

5.4. Ti-in-zircon thermometer

The concentration of Ti in zircon has been shown to be a function of the crystallization temperature and the activities of SiO_2 and TiO_2 in the parent melt (Watson et al., 2006; Ferry and Watson, 2007; Fu et al., 2008). In general, the Ti concentration in zircon appears to decrease from mafic to felsic rocks, which translates to decrease of Ti-in-zircon temperatures (Fu et al., 2008). Most zircons grains from the granitoid samples contain <7 ppm Ti (Table 3). Apparent temperatures for zircon crystallization were calculated using the Ti-in-zircon thermometer (Watson et al., 2006). The average apparent Ti-in-zircon temperatures are 599.25 and 651.4 °C for pegmatitic granites and trondhjemites respectively, indicating zircon grains derivation from a relatively cold granitic magma (Miller et al., 2003).

Table 4
U—Pb zircon dating data of the trondhjemite and pegmatitic granite rocks from the Penjween ophiolite complex.

Samples	concentrations (ppm)		Ratios												Age									
	U	Th	U/Th	Pb^{206}/Pb^{204}	Pb^{207}/Pb^{206}	2 s	Pb^{207}/U^{235}	2 s	Pb^{206}/U^{238}	2 s	Rho	Concordance	Pb^{208}/Th^{232}	2 s	Pb^{207}/Pb^{206}	2 s	Pb^{207}/U^{235}	2 s	Pb^{206}/U^{238}	2 s	Pb^{208}/Th^{232}	2 s	Pb^{206}/U^{238}	2 s
AA2																								
AA2_1	817	103.7	8.23	66	0.0471	0.0022	0.0461	0.0021	0.00706	0.00024	0.37563	105.4	0.00236	0.00018	73	88	45.7	2	45.4	1.5	47.7	3.6	141.643	4.815
AA2_2	574	55.6	10.38	11	0.0475	0.0017	0.047	0.0018	0.00705	0.00016	0.39699	106	0.00226	0.00028	83	71	46.6	1.7	45.3	1	45.6	5.7	141.844	3.219
AA2_3	745	112	6.7	84	0.0474	0.0024	0.0447	0.0023	0.00716	0.00018	0.29031	96.7	0.00222	0.00024	90	100	44.4	2.2	46	1.2	44.8	4.8	139.665	3.511
AA2_4	1600	154	10.44	129	0.0515	0.0018	0.0522	0.0018	0.00701	0.00022	0.2952	95.1	0.00363	0.00031	275	80	51.7	1.7	45	1.4	73.2	6.3	142.653	4.477
AA2_5	779	89.9	8.83	60	0.0667	0.0063	0.0691	0.0081	0.00716	0.00021	0.59813	99.4	0.00608	0.00089	730	170	65.7	6.8	46	1.4	122	18	139.665	4.096
AA2_6	3227	538	5.86	240	0.0489	0.0013	0.0524	0.0015	0.00811	0.00016	0.48343	86	0.00286	0.00015	142	56	52.1	1.5	52.1	1	57.6	2.9	123.305	2.433
AA2_7	1380	195	7.93	98	0.0791	0.0036	0.0855	0.0046	0.00765	0.00012	0.43464	94.46	0.00862	0.00079	1153	96	83	4.3	49.14	0.77	173	16	130.719	2.050
AA2_8	446	40.2	11.33	40	0.0469	0.0023	0.049	0.0025	0.00755	0.00029	0.47188	93	0.00312	0.00035	77	92	48.5	2.4	48.5	1.8	62.9	7	132.450	5.087
AA2_9	933	90.5	10.48	49	0.0461	0.0011	0.0457	0.0011	0.007086	0.000092	0.10247	112	0.00206	0.00014	25	46	45.5	1.1	45.51	0.59	41.7	2.8	141.123	1.832
AA2_10	660	64	9.4	90	0.0534	0.0039	0.0449	0.0033	0.00716	0.0004	0.40878	86.6	0.00311	0.00077	340	160	44.6	3.2	46	2.5	63	15	139.665	7.803
AA2_11	1146	130.8	8.52	47	0.0464	0.0011	0.0463	0.0011	0.00724	0.0001	0.31984	102	0.00217	0.00014	38	47	45.9	1.1	46.48	0.65	43.9	2.7	138.122	1.908
AA2_12	681	89.4	7.73	150	0.048	0.0018	0.0468	0.0017	0.0072	0.00013	0.2505	97	0.00235	0.00026	103	76	46.4	1.6	46.25	0.81	47.5	5.2	138.889	2.508
PNJ6																								
PNJ6_1	3476	545	6.48	260	0.04653	0.00067	0.04629	0.00068	0.007163	0.000078	0.33186	110	0.002172	0.000061	32	29	46	0.67	46.01	0.5	43.9	1.200	139.606	1.52
PNJ6_2	2100	197	11.11	131	0.0457	0.00092	0.03737	0.00073	0.007195	0.000095	0.17114	115	0.00223	0.00014	-4	39	37.24	0.72	46.21	0.61	45.1	2.900	138.985	1.84
PNJ6_3	3970	743	5.89	220	0.04758	0.00064	0.04809	0.00067	0.007173	0.000075	0.38271	124	0.002097	0.000073	83	28	47.75	0.65	46.07	0.48	42.3	1.500	139.412	1.46
PNJ6_4	3960	463	8.33	290	0.0438	0.0011	0.0432	0.0013	0.00711	0.00018	0.5103	114	0.00286	0.00013	−87	45	43	1.2	45.7	1.2	57.8	2.700	140.647	3.56
PNJ10																								
PNJ10_1	688	347.9	1.96	77	0.0499	0.0016	0.0935	0.0032	0.01388	0.00027	0.51513	86	0.00485	0.00023	184	65	90.7	3	88.9	1.7	97.9	4.6	72.04611	1.401473
PNJ10_2	1019	114	9.34	101	0.04737	0.00086	0.0923	0.0017	0.01412	0.00015	0.25032	93	0.00409	0.00019	71	37	89.6	1.6	90.41	0.97	82.5	3.8	70.82153	0.752353
PNJ10_3	972	102.3	9.81	87	0.0495	0.0013	0.0954	0.0019	0.01433	0.00023	0.16984	137	0.00433	0.00031	166	56	92.5	1.8	91.7	1.4	87.3	6.2	69.78367	1.120045
PNJ10_4	110.2	38.9	3.03	12.6	0.0474	0.0027	0.0938	0.0051	0.01429	0.00024	0.15654	111.4	0.00526	0.0005	90	110	90.6	4.7	91.5	1.5	106	10	69.97901	1.175295
PNJ10_5	349	27.1	12.94	42	0.0491	0.0013	0.0953	0.0029	0.01411	0.00026	0.50399	92	0.00411	0.00046	145	54	92.3	2.7	90.3	1.6	82.8	9.2	70.87172	1.305928
PNJ11																								
PNJ11_1	1320	167.8	7.2	159	0.0524	0.0019	0.1013	0.0048	0.01398	0.00051	0.66477	117	0.00471	0.00019	279	75	97.7	4.4	89.5	3.2	95	3.7	71.53076	2.609491

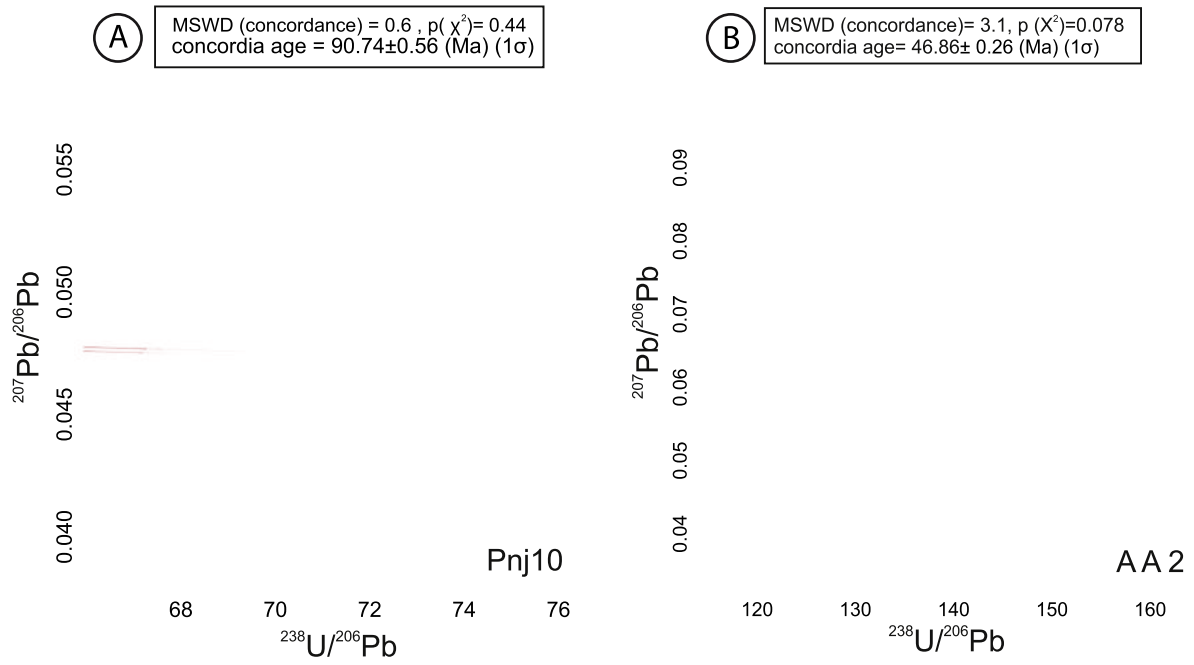

Fig. 8. U—Pb concordia diagrams of zircons from the pegmatitic granite intrusion (sample AA2), and the trondhjemite intrusion (sample PNJ-10) of the Penjween ophiolite complex.

5.5. (U—Th)/(He—Pb) double dating for zircon

Four granitoid samples were chosen for (U—Th)/(He—Pb) double dating, two from group-I trondhjemite rocks (PNJ-10 and PNJ-11) and two from group-II pegmatitic granite rocks (AA2 and PNJ-6). The zircon U—Pb analysis yielded early Late Cretaceous age for group-I trondhjemite rocks (90.74 ± 0.56 Ma ($n = 5$) for sample PNJ-10, and 89.5 ± 3.2 Ma ($n = 1$) for sample PNJ-11), and the middle Eocene age for group-II pegmatitic granite rocks (46.86 ± 0.26 Ma ($n = 9$) for sample AA2, and 45.9 ± 0.7 Ma ($n = 3$) for sample PNJ6) (Table 4; Fig. 8). These crystallization ages indicate that the POC underwent different magmatic events at two different times. To reveal the exhumation ages of these genetically different intrusions, four zircon grains from each of PNJ-10 and AA2 samples were selected for (U—Th)/He analysis. The age results showed 21.8 ± 4.9 Ma and 23.5 ± 3.4 Ma for PNJ-10 and AA2 samples, respectively (Table 5). These two analogous exhumation ages from both intrusions that have different crystallization ages suggest that the POC exhumed during the latest Oligocene-earliest Miocene time.

6. Discussion

6.1. Significance of zircon trace elements of the Penjween granitoid intrusions

Trace elements concentrations in zircon grains of the pegmatitic granite samples show enrichment in U, Th and Hf, and depletion in high field strength elements (e.g. Ti, Nb, and Ta) relative to their concentration in the zircon grains from the trondhjemite samples. Such variation in composition reflects differences in the origin of the granitic melts of the zircon grains. Richness in U and Th and depletion in high field strength elements indicative of S-Type granite, otherwise reflects I-type granite (Wang et al., 2012). In this study, the obvious positive Ce-anomalies, steep MREE-HREE patterns with high $(Lu/Gd)_N$ ratios of

Table 5
Zircon (U—Th)/(He—Pb) double dating data of the trondhjemite and pegmatitic granite rocks from the Penjween ophiolite complex.

Sample	Rock type	Mineral	~U-pb Age	Exhumation Age, Ma	Err., Ma	U (ppm)	Th (ppm)	147Sm (ppm)	[U]e	Th/U	He (nmol/g)	mass (ug)	Ft	ESR	
AA2-1	Pegmatite granite	Zircon	47.0	20.3	1.63	1269.4	107.9	13.1	1294.3	0.09	99.1	2.45	0.70	36.78	Avg: 23.47795
AA2-2	Pegmatite granite	Zircon	47.0	22.7	1.81	706.5	73.6	0.8	723.4	0.10	62.8	2.75	0.71	38.47	StD: 3.44288
AA2-3	Pegmatite granite	Zircon	47.0	22.5	1.80	420.8	64.0	2.6	435.5	0.15	37.0	2.40	0.70	37.15	
AA2-4	Pegmatite granite	Zircon	47.0	28.4	2.27	821.5	106.6	0.4	846.0	0.13	98.8	5.75	0.76	48.14	
PNJ10-1	Trondhjemite	Zircon	90.0	15.5	1.24	123.0	29.7	0.9	129.9	0.24	8.6	7.92	0.79	55.68	Avg:
PNJ10-2	Trondhjemite	Zircon	90.0	20.6	1.65	144.3	41.0	1.0	153.7	0.28	12.5	2.82	0.73	42.20	21.83051
PNJ10-3	Trondhjemite	Zircon	90.0	24.7	1.97	523.9	68.9	1.0	539.7	0.13	55.7	5.33	0.78	51.20	StD:
PNJ10-4	Trondhjemite	Zircon	90.0	26.6	2.13	764.3	29.9	1.5	771.2	0.04	84.8	5.07	0.77	48.64	4.90312
UTFCT2-1010	Standard	Zircon		25.7	2.06	175.7	94.4	1.5	197.4	0.54	22.0	9.61	0.80	60.26	
UTFCT2-1011	Standard	Zircon		26.5	2.12	236.6	108.5	3.0	261.6	0.46	30.2	10.20	0.81	61.11	

88 in zircons from pegmatitic granites to 71 in zircons from trondhjemites (Table 3; Fig. 7) confirm the igneous origin of both types (e.g., Belousova et al., 2002; Hoskin and Schaltegger, 2003). The total REE content and Eu-anomaly (Average $Eu/Eu^* = 0.29$) of the trondhjemite zircons suggest that these zircons were crystallized from mafic melts (Hoskin and Schaltegger, 2003; Grimes et al., 2009). Therefore, a possible source of the zircons from the Penjween granitoid intrusions could be either from a mantle-related source, or a subducted oceanic slab, or from both. For the pegmatitic granites, the trace elements in zircon show a positive Ce-anomaly, steep MREE-HREE with a negative Eu-anomaly (Average $Eu/Eu^* = 0.59$; Fig. 7). Published data reveals that igneous zircon grains derived from oceanic crustal rocks commonly show the same signatures (Grimes et al., 2009). The negative Eu-anomalies are due to the fact that plagioclase fractionation consumes Eu from the magma prior to or during zircon crystallization (Grimes et al., 2007). Accordingly, a reasonable source for the zircons in pegmatitic granite with the negative Eu-anomaly could be a subducted oceanic slab.

6.2. Origin of the Penjween granitoid intrusions

The whole-rock geochemistry of the Penjween granitoid intrusions show peraluminous characteristic indicated from the A/CNK ratio of ≥1.0 (Fig. 5A). Based on both geological and geochemical evidences (major, trace and REE), the granitoids display two different geochemical features (Fig. 5B), reflecting different magma generation events during the evolution of the POC. The trondhjemite rocks show some characteristics of adakites, with high SiO_2 (>66 wt%), Al_2O_3 (>18 wt%), and Na_2O (>8 wt%) contents, and high Sr/Y ratios of 10.46–36.7. Additionally, they are enriched in LREE and LILE, and have very low K_2O content of ≤0.14 wt%. Based on SiO_2 and K_2O relations (Peccerillo and Taylor, 1976), these trondhjemite intrusions were likely generated from basaltic tholeiite (Fig. 5C). The trondhjemite age of ~90 Ma gives the minimum age of the ultramafic section of the POC. In other words, it indicates that ~90 Ma ago, the ultramafic section of the Penjween ophiolite complex was already underlain by a source capable of yielding silica-saturated sodic granitoids. Two origins of such sodic granitoids are possible (1) a plagiogranite sensu stricto that was crystallized from late melt fractions of mafic magmas, particularly MORB (e.g. Coleman and Peterman, 1975; Floyd et al., 1998), and (2) melting of mafic rocks in a subduction channel at high pressure with amphibole as the main residual mineral (Li and Li, 2003). Given that the trondhjemites are intruded into upper mantle section of the POC, they are probably subduction-type granites. This type is common in ophiolite sequences and resembles typical adakites.

The Eocene pegmatitic granite rocks are different in their geochemical properties. They display high K_2O content (average 5.73 wt%) and relatively low Na contents (average 3.68 wt%). The low Na contents suggest that the pegmatitic granite was formed at relatively low pressure (Patiño Douce and Harris, 1998). The relationship between SiO_2 and K_2O, indicates that these rocks crystalized were from a high-K calc alkaline to shoshonitic magma (Peccerillo and Taylor, 1976; Fig. 5C). These geochemical data along with zircon U—Pb age of ~46 Ma suggest that the pegmatitic granite intrusion was not only generated from a younger melting event, but also was derived from a different non-mafic source. The highly potassic character of the pegmatitic granite indicates a low temperature melting event that involves incongruent breakdown of micas, pointing most likely to a sedimentary source at depth.

6.3. Timing of generation and exhumation of the Penjween ophiolite complex

The aforementioned results and interpretations indicate that the POC was intruded first by the early Late Cretaceous (~90 Ma ago) trondhjemite dykes and later by the middle Eocene (~46 Ma ago) pegmatitic granite dykes. Both sets of the granitic rocks show similar zircon (U—Th)/He exhumation ages of the latest Oligocene to earliest Miocene (~23 Ma). The trondhjemite rocks (~90 Ma) are interpreted as subduction-type granites that were formed in the lower crust, and the pegmatitic granite rocks (~46 Ma) with high potassic character were formed from a sedimentary rock-rich source at shallower depth. This synthesis suggests that after generation of the ultramafic section of the POC in the early Late Cretaceous, the POC underwent further magmatism in the middle Eocene probably due to melting of sedimentary rocks from the downgoing Neotethyan oceanic slab. Such tectonic history led to presence of two genetically different granitoid bodies within the POC. Subsequently during the latest Oligocene-earliest Miocene time (~23 Ma), the POC was exhumed as a consequence of the Arabian-Eurasian continental collision during Oligocene (Agard et al., 2005; Pirouz et al., 2017; Koshnaw et al., 2018).

6.4. Geodynamic evolution of the Arabia-Eurasia collision zone in the NW Zagros

The geodynamic evolution of the Zagros Suture Zone is complex due to multiple phases of tectonic deformation events throughout its history such as subduction, obduction, arc-continent collision and continent-continent collision. The Zagros orogenic belt was formed as a result of the closure of the Neotethys ocean between the Arabian and Eurasian plates (Alavi, 1994; Talbot and Alavi, 1996; Stampfli and Borel, 2002; Shafaii Moghadam and Stern, 2015). The POC, along with the other ophiolitic terranes in the Kurdistan region of Iraq, are allochthonous sheets that were derived from the Neotethys oceanic crust and emplaced onto of the Arabian plate margin (Jassim and Goff, 2006; Ali et al., 2014, 2019; Ismail et al., 2014, 2017). The Penjween granitoid intrusions show different origins at different times, but with similar time of exhumation. These new informations can be integrated with the previously published data to enhance the tectonic evolution model of the Arabian-Eurasian convergent margin in the NW Zagros orogenic belt.

During the late Tithonian-early Cretaceous, the Neotethys ocean commenced to spread and an oceanic-oceanic subduction zone initiated (Hallam, 1976; Agard et al., 2005; Saccani et al., 2013, 2017; Stern and Gerya, 2018). The formation of this subduction zone was accompanied by the extension-induced arcs (intra-oceanic arcs). These arc complexes (basaltic andesites and andesites) are represented by the 106–92 Ma old Hasanbag ophiolitic arc in NE Iraq (Ali et al., 2012), the Urumieh Dokhtar arc in Iran (Shafaii Moghadam and Stern, 2011), and the Cenomanian Yuksekova complexes in the SE Turkey (Ural et al., 2015). The new results from this study suggest that the POC was formed during the early Late Cretaceous (~90 Ma) or earlier and is related to the other Cretaceous ophiolite assemblages in the Middle East. This interpretation is in agreement with the previously reported U—Pb zircon age of 93.8 ± 0.7 Ma for plagiogranite rocks from the Penjween area (Abdulla, 2015). During the Late Cretaceous, ophiolitic intra-oceanic arcs collided with the Arabian continental passive margin (Saccani et al., 2013 and references therein). This collision resulted in the obduction of the Neotethys oceanic crust onto the northeastern margin of the Arabian Plate (Alavi, 1994; Mohaijel et al., 2003; Agard et al., 2005; Saura et al., 2011; Ali et al., 2012; Shafaii Moghadam and Stern, 2015; Barber et al., 2019).

During the middle Eocene (~46 Ma) granitoids intruded into the POC, likely generated from the remnant of the downgoing Neotethyan oceanic slab below the obducted ophiolitic rocks. In the POC, there are evidences suggesting that the subducted Arabian continental plate was partially melted as indicated from the peraluminous potassic granitic magma (shoshonite).

After the closure of the Neotethys ocean, the POC was emplaced onto the Walash-Naopurdan groups during the latest Oligocene-earliest Miocene, as evidenced from the zircon (U—Th)/He exhumation age of ~23 Ma, likely by out-of-sequence thrusting (Ali et al., 2014). Based on apatite fission track (AFT) analysis on samples from the basement outcrop in the Misho mountains, NW Iran and NE of the study area, a corresponding exhumation age of ~21–22 Ma has also been reported

(Behyari et al., 2017). According to the nature of the POC lower contact, the Walash-Naopurdan thrust sheets are missing in Penjween area (Figs. 2, 3), but they are exposed in the Mawat area and thrusted onto the Red Bed Series deposits. Such relationship implies that the Walash-Naopurdan thrust sheets are either completely covered by the POC or they were absent at that locality during the ophiolite complex obduction. In case of being thrusted and covered by the POC, the Walash-Naopurdan thrust sheets must have been thrusted on the Red Bed Series prior to or coeval with the ~23 Ma event of the POC thrusting.

7. Conclusions

1. New zircon U—Pb ages of granitoid intrusions from the northwestern Zagros Penjween ophiolite complex in the suture zone of Arabia-Eurasia point at two phases of felsic magmatism. These phases include the intra-oceanic subduction in the early Late Cretaceous (~90 Ma) and the involvement of buried sedimentary rocks that was associated with the down going slab in the middle Eocene magmatism (~46 Ma). Based on the zircon (U—Th)/(He—Pb) double dating, these two genetically dissimilar rock bodies were both exhumed at comparable time during the latest Oligocene–earliest Miocene (~23 Ma), possibly due to the collision of the Arabian and Eurasian continental plates.
2. The trondhjemites age of ~90 Ma gives the minimum age of the ultramafic section of the Penjwen ophiolite complex and indicates that ~90 Ma ago the ultramafic rocks were already underlain by a source capable of yielding silica-saturated sodic granitoids.
3. The Eocene pegmatitic granite (~46 Ma) is different in its geochemical characteristics compared to the late Cretaceous trondhjemite (~90 Ma). The Eocene rocks are potassic pegmatitic granites; as such, they represent not only a younger melting event, but also derivation from a different non-mafic source. The highly potassic character of pegmatitic granite suggests low temperature melting, involving incongruent breakdown of micas, pointing at a sedimentary source at depth.

Supplementary data to this article can be found online at https://doi.org/10.1016/j.lithos.2020.105714.

Declaration of Competing Interest

The authors declare that they have no known competing financial interests or personal relationships that could have appeared to influence the work reported in this paper.

Acknowledgments

We acknowledge the support that were given by the Kirkuk University and appreciate the helpful comments by the anonymous reviewers as well as the editor in chief (Michael Roden) that improved the manuscript.

References

Abdulla, K.L., 2015. Petrogenesis and Geochronology of Plagiogranite Rocks in Penjween Ophiolite, Kurdistan Region, NE Iraq. Unpublished MSc. Thesis. University of Sulaimani (pp. 88).

Agard, P., Omrani, J., Jolivet, L., Mouthereau, F., 2005. Convergence history across Zagros (Iran): constraints from collisional and earlier deformation. Int. J. Earth Sci. 94, 401–419.

Alavi, M., 1994. Tectonics of the Zagros orogenic belt of Iran: new data and interpretations. Tectonophysics 229, 211–238.

Al Hassan, M.E., Hubbard, F.H., 1985. Magma segregation in the tectonic remnant of basalt ophiolite, Penjween, NE Iraq. Ofioliti 10, 139–146.

Al Humadi, H., Vaisanen, M., Ismail, S.A., Kara, J., O'Brien, H., Lahaye, Y., Lehtonen, M., 2019. U-Pb geochronology and Hf isotope data from the late cretaceous Mawat ophiolite, NE Iraq. Heliyon 5, e02721.

Al-Kadhimi, J., Sissakian, V.K., Fattah, A.S., Deikran, D.B., 1996. Tectonic Map of Iraq, Scale 1: 1000 000. second ed. GEOSURV, Baghdad, Iraq.

Al-Qayim, B., Omer, A., Koyi, H., 2012. Tectonostratigraphic overview of the Zagros suture zone, Kurdistan region, Northeast Iraq. GeoArabia 17 (4), 109–156.

Ali, S.A., Mohajjel, M., Aswad, K.J., Ismail, S.A., Buckman, S., Jones, B.G., 2014. Tectono-stratigraphy and general structure of the northwestern Zagros collision zone across the Iraq-Iran border. J. Environ. Earth Sci. 4 (4) 92e110.

Ali, S.A., Buckman, S., Aswad, K.J., Jones, B.G., Ismail, S.A., Nutman, A.P., 2012. Recognition of Late Cretaceous Hasanbag ophiolite-arc rocks in the Kurdistan region of the Iraqi Zagros thrust zone: a missing link in the paleogeography of the closing Neo-Tethys Ocean. Lithosphere 4, 395–410.

Ali, S.A., Ismail, S.A., Nutman, A.P., Bennett, V.C., Jones, B.G., Buckman, S., 2016. The intra-oceanic Cretaceous (~108 Ma) Kata-Rash arc fragment in the Kurdistan segment of Iraqi Zagros suture zone: implications for Neotethys evolution and closure. Lithos 260, 154–163.

Ali, S.A., Nutman, A.P., Aswad, K.J., Jones, B.G., 2019. Overview of the tectonic evolution of the Iraqi Zagros thrust zone: sixty million years of Neotethyan ocean subduction. J. Geodyn. 129, 162–177.

Arai, S., Shimzu, Y., Ismail, S.A., Ahmed, A.H., 2006. Low-T formation of high-Cr spinel with apparently primary chemical characteristics within podiform chromitite from Rayat, northeastern Iraq. Mineral. Mag. 70, 499–508.

Barber, D.E., Stockli, D.F., Galster, F., 2019. The Proto-Zagros Foreland Basin in Lorestan, Western Iran: insights from multimineral detrital geothermochronometric and trace elemental provenance analysis. Geochem. Geophys. Geosyst. 20 (6), 2657–2680.

Behyari, M., Mohajjel, M., Sobel, E.R., Rezaeian, M., Moayyed, M., Schmidt, A., 2017. Analysis of exhumation history in Misho Mountains, NW Iran: insights from structural and apatite fission track data. N. Jb. Geol. Paläont. (Abh.) 283 (3), 291–308.

Belousova, E.A., Walters, S., Griffin, W.L., O'Reilly, S.Y., Fisher, N.I., 2002. Zircon trace-element compositions as indicators of source rock type. Contrib. Mineral. Petrol. 143 (5), 602–622.

Buday, T., Jassim, S.Z., 1987. The Regional Geology of Iraq. Tectonism, Magmatism and Metamorphism. Iraq Geological Survey Baghdad part 2. (pp. 351).

Coleman, R.G., Donato, M.M., 1979. Oceanic plagiogranite revisited. In: Barker, F. (Ed.), Trondhjemites, Dacites and Related Rocks. Elsevier, Amsterdam, pp. 149–168.

Coleman, R.G., Peterman, Z.E., 1975. Oceanic plagiogranite. J. Geophys. Res. 80, 1099–1108.

Dercourt, J., Zonenshain, L.P., Ricou, L.-E., Kazmin, V.G., Le Pichon, X., Knipper, A.L., Grandjacquet, C., Sbortshikov, I.M., Geyssant, J., Lepvrier, C., Perchersky, D.H., Boulin, J., Sibuet, J.-C., Savostin, L.A., Sorokhtin, O., Westphal, M., Bazhenov, M.L., Lauer, J.P., Biju Duval, B., 1986. Geological evolution of the Tethys from the Atlantic to the Pamirs since the Lias. In: Auboin, J., Le Pichon, X., Monin, A.S. (Eds.), Evolution of the Tethys. Tectonophysics. 123, pp. 241–315.

Falcon, N.L., 1974. Southern Iran: Zagros Mountains. 41. Geol. Soc. Lond. Spec. Publ., pp. 199–211.

Farley, K.A., Wolf, R.A., Silver, L.T., 1996. The effects of long alpha-stopping distances on (U/Th)/He ages. Geochim. Cosmochim. Acta 60 (21), 4223–4229.

Fergusson, C.L., Nutman, A.P., Mohajjel, M., Bennett, V.C., 2016. The Sanandaj–sirjan Zone in the Neo-Tethyan suture, western Iran: zircon U-Pb evidence of Late Palaeozoic rifting of northern Gondwana and mid-Jurassic orogenesis. Gondwana Res. 40, 43–57.

Ferry, J.M., Watson, E.B., 2007. New thermodynamic models and revised calibrations for the Ti-in688 zircon and Zr-in-rutile thermometers. Contrib. Mineral. Petrol. 154, 429–437.

Floyd, P.A., Yaliniz, M.K., Goncuoglu, M.C., 1998. Geochemistry and petrogenesis of intrusive and extrusive ophiolitic plagiogranites, central Anatolian Crystalline Complex, Turkey. Lithos 42, 225–241.

Fu, B., Page, F.Z., Cavosie, A.J., Clechenko, C.C., Fournelle, J., Kita, N.T., Lackey, J.S., Wilde, S. A., Valley, J.W., 2008. Ti-in-zircon thermometry: applications and limitations. Contrib. Mineral. Petrol. 156, 197–215.

Gehrels, G., 2011. Detrital zircon U-Pb geochronology: current methods and new opportunities. Tectonics of Sedimentary Basins: Recent Advances, pp. 45–62.

Gehrels, G.E., Valencia, V.A., Ruiz, J., 2008. Enhanced precision, accuracy, efficiency, and spatial resolution of U-Pb ages by laser ablation–multicollector–inductively coupled plasma–mass spectrometry. Geochem. Geophys. Geosyst. 9 (3).

Grimes, C.B., John, B.E., Cheadle, M.J., Mazdab, F.K., Wooden, J.L., Swapp, S., Schwartz, J.J., 2009. On the occurrence, trace element geochemistry, and crystallization history of zircon from in situ ocean lithosphere. Contrib. Mineral. Petrol. 158, 757–783.

Grimes, C.B., John, B.E., Kelemen, P.B., Mazdab, F., Wooden, J.L., Cheadle, M.J., Hanghøj, K., Schwartz, J.J., 2007. The trace element chemistry of zircons from oceanic crust: a method for distinguishing detrital zircon provenance. Geology 35, 643–646.

Hallam, A., 1976. Geology and plate tectonics interpretation of the sediments of the Mesozoic radiolarite-ophiolite complex in the Neyriz region, southern Iran. Geol. Soc. Am. Bull. 87, 47–52.

Hanchar, J.M., Westrenen, W.V., 2007. Rare earth element behavior in zircon-melt systems. Elements 3, 37–42.

Hinton, R.W., Upton, B.G.J., 1991. The chemistry of zircon: variations within and between large crystals from syenite and alkali basalt xenoliths. Geochim. Cosmochim. Acta 55, 3287–3302.

Hoskin, P.W.O., Schaltegger, U., 2003. The composition of zircon and igneous and metamorphic petrogenesis. In: Hanchar, J.M., Hoskin, P.W.O. (Eds.), Zircon. Rev. Mineral. Geochem.. vol. 53, pp. 27–62

Ismail, S.A., Ali, S.A., Nutman, A.P., Bennett, V.C., Jones, B.G., 2017. The Pushtashan juvenile suprasubduction zone assemblage of Kurdistan (northeastern Iraq): a Cretaceous (Cenomanian) Neo-Tethys missing link. Geosci. Front. 8, 1073–1087.

Ismail, S.A., Arai, S., Ahmed, A.H., Shimizu, Y., 2009. Chromitite and peridotite from Rayat, northeastern Iraq, as afragment of Tethyan ophiolite. Island Arc 18, 175–183.

Ismail, S.A., Kettanah, Y.A., Chalabi, S.N., Ahmed, A.H., Arai, S., 2014. Petrogenesis and PGE distribution in the Al- and Cr-rich chromitites of the Qalander ophiolite, northeastern

Iraq: implications for the tectonic environment of the Iraqi Zagros Suture Zone. Lithos 202-203, 21–36.
Ismail, S.A., Tola, M.M., Paul, F.C., 2010. Platinum-group elements geochemistry in podiform chromitites and associated peridotites of the Mawat ophiolite, northeastern Iraq. J. Asian Earth Sci. 37, 31–41.
Jackson, S.E., Pearson, N.J., Griffin, W.L., Belousova, E.A., 2004. The application of laser ablation-inductively coupled plasma-mass spectrometry to in situ U–Pb zircon geochronology. Chem. Geol. 211, 47–69.
Jassim, S.Z., Goff, J.C., 2006. Geology of Iraq. Dolin, Prague, Moravian Museum, Brno, Czech Republic (pp. 341).
Koshnaw, R.I., Horton, B.K., Stockli, D.F., Barber, D.E., Tamar-Agha, M.Y., 2019. Sediment routing in the Zagros foreland basin: drainage reorganization and a shift from axial to transverse sediment dispersal in the Kurdistan region of Iraq. Basin Res. 1–28.
Koshnaw, R.I., Horton, B.K., Stockli, D.F., Barber, D.E., Tamar-Agha, M.Y., Kendall, J.J., 2017. Neogene shortening and exhumation of the Zagros fold-thrust belt and foreland basin in the Kurdistan region of northern Iraq. Tectonophysics 694, 332–355.
Koshnaw, R.I., Stockli, D.F., Schlunegger, F., 2018. Timing of the Arabia-Eurasia continental collision—evidence from detrital zircon U-Pb geochronology of the Red Bed Series strata of the northwest Zagros hinterland, Kurdistan region of Iraq. Geology 47, 47–50.
Lawa, F.A., Koyi, H., Ibrahim, A., 2013. Tectono-stratigraphic evolution of the NW segment of the Zagros fold-thrust belt, Kurdistan, NE Iraq. J. Pet. Geol. 36, 75–96.
Lecuyer, C., Grandjean, P., O'Neil, J.R., Cappetta, H., Martineau, F., 1990. Thermal excursion in the ocean at the Cretaceous-Tertiary boundary (northern Morocco): S18O record of phosphatic fish debris. Palaeogeogr. Palaeoclimatol. Palaeoecol. 105, 235–243.
Li, W.X., Li, X.H., 2003. Adakitic granites within the NE Jiangxi ophiolites, South China: geochemical and Nd isotopic evidence. Precambrian Res. 122, 29–44.
Linnen, R.L., Samson, I.M., Williams-Jones, A.E., Chakhmouradian, A.R., 2014. Geochemistry of the rare-earth element, Nb, Ta, Hf, and Zr deposits. Treatise on Geochemistry, 2nd edition, pp. 543–567.
Marsh, J.H., Stockli, D.F., 2015. Zircon U–Pb and trace element zoning characteristics in an anatectic granulite domain: insights from LASS-ICP-MS depth profiling. Lithos 239, 170–185.
McDonough, W.F., Sun, S.-S., 1995. The composition of the earth. Chem. Geol. 120, 223–253.
Miller, C.F., Mcdowell, S.M., Mapes, R.W., 2003. Hot and cold granites? Implications of zircon saturation temperatures and preservation of inheritance. Geology 31, 529–553.
Mohajjel, M., Fergusson, C.L., 2014. Jurassic to Cenozoic tectonics of the Zagros Orogen in northwestern Iran. Int. Geol. Rev. 56, 263–287.
Mohajjel, M., Fergusson, C.L., Sahandi, M.R., 2003. Cretaceous-Tertiary convergence and continental collision, Sanandaj–Sirjan Zone, western Iran. J. Asian Earth Sci. 21, 397–412.
Numan, N.M., 1997. A plate tectonic scenario for the Phanerozoic successions in Iraq. Iraqi Geol. J. 30, 85–110.
O'Connor, J.T., 1965. A classification of quartz rich igneous rock based on feldspar ratios. USGS 525B, B79–B84.
Patiño Douce, A.E., Harris, N., 1998. Experimental constraints on Himalayan anatexis. J. Petrol. 39, 689–710.
Paton, C., Hellstrom, J., Paul, B., Woodhead, J., Hergt, J., 2011. Iolite: freeware for the visualisation and processing of mass spectrometric data. J. Anal. Atom. Spectrom. 26, 2508–2518.
Peccerillo, R., Taylor, S.R., 1976. Geochemistry of Eocene calc-alkaline volcanic rocks from the Kastamonu area, northern Turkey. Contrib. Mineral. Petrol. 58, 63–81.
Petrus, J.A., Kamber, B.S., 2012. Vizual Age: a novel approach to laser ablation ICP-MS UPb geochronology data reduction. Geostand. Geoanal. Res. 36, 247–270.
Pirouz, M., Avouac, J.P., Hassanzadeh, J., Kirschvink, J.L., Bahroudi, A., 2017. Early Neogene foreland of the Zagros, implications for the initial closure of the Neo-Tethys and kinematics of crustal shortening. Earth Planet. Sci. Lett. 477, 168–182.
Reiners, P.W., Campbell, I.H., Nicolescu, S., Allen, C.M., Hourigan, J.K., Garver, J.I., et al., 2005. (U-Th)/(He-Pb) double dating of detrital zircons. Am. J. Sci. 305, 259–311.
Reiners, P.W., Farley, K.A., Hickes, H.J., 2002. He diffusion and (U-Th)/He thermochronometry of zircon: initial results from fish Canyon Tuff and Gold Butte. Tectonophysics 349, 297–308.
Rubatto, D., Hermann, J., 2007. Zircon behaviour in deeply subducted rocks. Elements 3, 31–35.
Saccani, E., Allahyari, K., Beccaluva, L., Bianchini, G., 2013. Geochemistry and petrology of the Kermanshah ophiolites (Iran): implication for the interaction between passive rifting, oceanic accretion, and OIB-type components in the southern Neo-Tethys Ocean. Gondwana Res. 24, 392–411.
Saccani, E., Dilek, Y., Photiades, A., 2017. Time progressive mantle—melt evolution and magma production in a Tethyan marginal sea: a case study of the Albanide-Hellenide ophiolites. Lithosphere 10, 35–53.
Saura, E., Vergés, J., Homke, S., Blanc, E., Serra-Kiel, J., Bernaola, G., Casciello, E., Fernández, N., Romaire, I., Casini, G., Embry, J.C., 2011. Basin architecture and growth folding of the NW Zagros early foreland basin during the Late Cretaceous and early Tertiary. J. Geol. Soc. Lond. 168 (1), 235–250.
Shafaii Moghadam, S., Corfu, F., Chiaradia, M., Stern, R.J., Ghorbani, G., 2014. Sabzevar Ophiolite, NE Iran: progress from embryonic oceanic lithosphere into magmatic arc constrained by new isotopic and geochemical data. Lithos 210–211, 224–241.
Shafaii Moghadam, H., Corfu, F., Stern, R.J., Lotfibakhsh, A., 2019. The Eastern Khoy metamorphic complex of NW Iran: a Jurassic ophiolite or continuation of the Sanandaj-Sirjan Zone. J. Geol. Soc. Lond. 176, 517–529.
Shafaii Moghadam, H., Stern, R.J., 2011. Geodynamic evolution of upper Cretaceous Zagros ophiolites: formation of oceanic lithosphere above a nascent subduction zone. Geol. Mag. 148, 762–801.
Shafaii Moghadam, H., Stern, R.J., 2015. Ophiolites of Iran: Keys to understanding the tectonic evolution of SW Asia: (II) Mesozoic ophiolites. J. Asian Earth Sci. 100, 31–59.
Shand, S.J., 1943. The Eruptive Rocks. second ed. John Wiley, New York (444 pp.).
Soto-Kerans, G.M., Stockli, D.F., Janson, X., Lawton, T.F., Covault, J.A., 2020. Orogen proximal sedimentation in the Permian foreland basin. Geosphere 16 (2), 567–593.
Spooner, E.T.C., Fyfe, W.S., 1973. Sub-seafloor metamorphism, heat and mass transfer. Contrib. Mineral. Petrol. 42, 287–304.
Stampfli, G.M., Borel, G.D., 2002. A plate tectonic model for the Paleozoic and Mesozoic constrained by dynamic plate boundaries and restored synthetic oceanic isochrons. Earth Planet. Sci. Lett. 196, 17–33.
Stern, R.J., Gerya, T., 2018. Subduction initiation in nature and models: a review. Tectonophysics 746, 173–198.
Sun, S.-S., McDonough, W.F., 1989. Chemical and isotope systematics of oceanic basalts: implications for mantle composition and processes. In: Saunders, A.D., Norry, M.J. (Eds.), Magmatism in the Ocean Basins. 42. Geol. Soc. Spec. Publ., pp. 313–345.
Talbot, C.J., Alavi, M., 1996. The past of a future syntaxis across the zagros. In: Alsop, G.I., Blundell, D.J., Davison, I. (Eds.), Salt Tectonics. vol. 100. Geol. Soc. London, Spec. Pub., pp. 89–109.
Wang, K.X., Chen, P.R., Chen, W.F., Ling, H.F., Zhao, K.D., Yu, Z.Q., 2012. Magma mingling and chemical diffusion in the Taojiang granitoids in the Hunan Province, China: evidences from petrography, geochronology and geochemistry. Mineral. Petrol. 106, 164–243.
Watson, E.B., Wark, D.A., Thomas, J.B., 2006. Crystallization thermometers for zircon and rutile. Contrib. Mineral. Petrol. 15, 413–433.
Whitehouse, M.J., Platt, J.P., 2003. Dating high-grade metamorphism-constraints from rare-earth elements in zircons and garnet. Contrib. Mineral. Petrol. 145, 61–74.
Wolfe, M.R., Stockli, D.F., 2010. Zircon (U-Th)/He thermochronometry in the KTB drill hole, Germany, and its implications for bulk He diffusion kinetics in zircon. Earth Planet. Sci. Lett. 295, 69–82.